

Full paper

ZnO/ZnFe₂O₄/N-doped C micro-polyhedrons with hierarchical hollow structure as high-performance anodes for lithium-ion batteries

Yuan Ma^{a,b}, Yanjiao Ma^{a,b}, Dorin Geiger^c, Ute Kaiser^c, Huang Zhang^{a,b}, Guk-Tae Kim^{a,b}, Thomas Diemant^d, R. Jürgen Behm^{a,d}, Alberto Varzi^{a,b,*}, Stefano Passerini^{a,b,*}

^a Helmholtz Institute Ulm (HIU), Helmholtzstrasse 11, D-89081 Ulm, Germany

^b Karlsruhe Institute of Technology (KIT), P.O. Box 3640, D-76021 Karlsruhe, Germany

^c Central Facility for Electron Microscopy, Group of Electron Microscopy of Materials Science, Ulm University, Albert-Einstein-Allee 11, D-89081 Ulm, Germany

^d Institute of Surface Chemistry and Catalysis, Ulm University, Albert-Einstein-Allee 47, D-89081 Ulm, Germany

ARTICLE INFO

Keywords:

Hierarchical hollow micro-polyhedrons

Bi-component ZnO/ZnFe₂O₄

Nitrogen-doped carbon matrix

Metal-organic frameworks

Lithium-ion batteries

In situ XRD diffraction

ABSTRACT

In this work, a facile and potentially scalable self-template synthesis of bi-component ZnO/ZnFe₂O₄/N-doped C micro-polyhedrons with hierarchical hollow structure (ZZFO-C) is presented. These are obtained through calcination of a single bi-metallic metal-organic framework (MOF) precursor (ZIF-ZnFe, molar ratio of 3:1). The resulting material shows a high surface area and is constituted by the organized assembly of numerous nanoparticles sub-unit (with size in the range of 20 nm). By tuning the annealing conditions, porous ZnO/ZnFe₂O₄ (ZZFO) micro-polyhedrons are obtained. The ZZFO-C composite materials are studied as anodes for LIBs exhibiting remarkable energy storage performance, such as, large reversible capacity (ca. 1000 mA h g⁻¹ after 100 cycles at 200 mA g⁻¹), excellent rate capability and cycling stability. After high-rate capacity testing (1000 cycles at 2.0 A g⁻¹), ZZFO-C shows an excellent reversible capacity of 620 mA h g⁻¹. The excellent performance of ZZFO-C arises from its unique hierarchical hollow structure and the synergy between the two active components and the N-doped carbon matrix. The electrochemical reaction mechanism and structure phase changes upon the initial lithiation are identified via in situ X-ray diffraction studies.

1. Introduction

To face the increasing environmental issues and shortage of fossil fuels, scientists and engineers are committed to develop highly efficient energy storage technologies enabling greener and more sustainable energy supplies. In this regard, lithium-ion batteries (LIBs) play a vital role as energy source for next-generation electric vehicles and portable electronics, such as smart phones, laptops, smart glasses, etc. [1–4]. Nowadays, commercial LIBs make use of graphite-based anodes, however, possessing relatively low specific capacity and potential safety issues [1,5,6]. Therefore, the extensive exploration and ad-hoc design for new anodes materials are urgently needed in order to enhance the electrochemical performance and reduce the cost and safety hazards. Interestingly, low-cost and widely available transition metal oxides (TMOs) show huge potential as anode materials for LIBs due to the large specific capacity arising by different lithiation processes, such as conversion (e.g., Fe₂O₃) and/or alloying reaction (ZnO, SnO₂) [1,2,7]. MTMOs, i.e., mixed transition metal oxide such as A₂B_{3–x}O₄, where A and B are two different metals (e.g., ZnFe₂O₄), can boost the

electrochemical performance of LIBs owing to the synergy between conversion and alloying [2,5,7]. Nevertheless, the low electronic conductivity, slow ion diffusion kinetics and poor cycling stability resulting from continuous volumetric changes and serious metal oxides aggregation, has limited so far the application of such TMOs- and MTMOs-based anodes [6,8].

To address the above-mentioned issues, many strategies have been proposed recently, including the design of advanced TMOs- and MTMOs-based electrodes. One of the most effective strategies is to fabricate well-organized hierarchical micro-/nano-structures constituted by secondary superstructures built from an ordered assembly of nanoparticles [2,5,8]. TMOs and MTMOs with hierarchical structure benefit from both the nanometer-sized structure (e.g., nanoparticles, nanosheets, and nanorods) and micro-/submicro-sized assemblies (such as mesoporous microcubes [5], hollow microspheres [9], ball-in-ball microspheres [10], mesoporous spindle-like microstructure [11]), which provide cushion-like space to accommodate structural strain and enhance the contact area between electrode and electrolyte [2,5,8–11]. By means of carbon coatings or embedding in a carbon matrix

* Corresponding author at: Helmholtz Institute Ulm (HIU), Helmholtzstrasse 11, D-89081 Ulm, Germany.

E-mail addresses: alberto.varzi@kit.edu (A. Varzi), stefano.passerini@kit.edu (S. Passerini).

(eventually doped with heteroatoms such as, e.g., nitrogen, sulfur or phosphor), the lithium ion storage performance of TMOs and MTMOs can be also further improved [6,12–14]. The carbon layer/matrix has two positive roles. It acts as a buffer layer to alleviate volumetric variation, preventing its pulverization, and improves the electrical conductivity [6,8,12,13]. Meanwhile, the heteroatom-doped carbon layer/matrix can bring further positive effects (such as additional Li storage sites, better electrode/electrolyte wettability, improved electrical conductivity, etc.), resulting in an improved cycling stability, specific capacity, and rate performance [14].

The development of TMOs constituted of two active alloying metals (MTMOs) is also a promising approach to obtain high performance LIBs anode materials [7]. Two different TMOs or MTMOs can be uniformly assembled into hierarchical micro-/nano-hybrids [5], such as ZnO/ZnCo₂O₄ [15], CoO/CoFe₂O₄ [16], NiCo₂O₄/MnO₂ [17], Co₃O₄/CoFe₂O₄ [18], and ZnO/ZnFe₂O₄ [5,8] offering, in all cases, better energy storage performance than the single components. Among numerous TMOs and MTMOs, ZnO and ZnFe₂O₄ have emerged as highly promising anode materials because of their large theoretical capacity (981 mA h g⁻¹ and 1072 mA h g⁻¹, respectively), low toxicity, and cost, i.e., high abundance [5,12]. The excellent electrochemical activity of ZnO and ZnFe₂O₄ is ascribed to the synergy between conversion and alloying [12,19]. Based on all above benefits, the fabrication of hierarchical structures composed of ZnO and ZnFe₂O₄ coated or incorporated in heteroatom-doped carbon layer/matrix composite as anode materials appears as a promising approach to improve LIBs performance.

Metal-organic frameworks (MOFs), produced combining an organic component (organic ligands or organometallic complexes) with inorganic moieties (metal clusters or ions) by covalent coordination linkages or other interaction (e.g., π - π stacking, H-bond, and van der Waals forces), are a novel type of porous materials with large surface area, and huge pores' volume [20–23]. Based on these characteristics, MOFs have been employed for several purposes from gas separation/storage, to catalysis and drug delivery [20–22]. Especially in energy storage, MOFs have been proposed as promising template precursors for hierarchical TMOs or MTMOs with various morphologies. For example, Lou et al. reported hierarchical structured Fe₂O₃ micro-boxes, made through annealing Prussian blue (PB), showing high specific capacity (950 mA h g⁻¹ at 200 mA g⁻¹) [24]. Regarding bi-component TMOs & MTMOs, Wang and co-workers reported Fe₂O₃@NiCo₂O₄ porous nano-cages produced by heating core-shell Ni-Fe-Co MOFs in air. The reversible capacity of this material could reach 1079.6 mA h g⁻¹ (exceeding its theoretical capacity) after 100 cycles [25]. Li and co-workers successfully synthesized Fe₂O₃/Co₃O₄ hollow micro-cubes with double-shell, via calcination of the PB/Co(OH)₂ composite precursor [26]. This latter composite displayed an excellent LIB anode performance resulting from the synergistic effect of Fe₂O₃ and Co₃O₄ [26]. Zou et al. and Yuan's group also reported porous ZnO/ZnFe₂O₄/C and ZnO/ZnFe₂O₄ prepared by annealing of bi-metal MOF (with terephthalic acid as organic ligands) and PB, respectively, both exhibiting good performance for LIBs (respectively 837 and 988 mA h g⁻¹ after 100 cycles) [5,8]. All these reports show that TMOs and MTMOs derived from MOFs have a huge potential as advanced material for LIBs anodes. In spite of some studies about MOFs derived bi-component active metal oxides, it is still a huge challenge to build advanced structural ZnO/ZnFe₂O₄, especially included in heteroatom-doped carbon layer/matrix. To the best of our knowledge, hierarchical bi-component ZnO/ZnFe₂O₄ derived from zeolitic imidazolate frameworks (ZIFs, an important subclass of MOFs) have not been reported so far. The appeal of such kind of MOFs arises from the organic ligands that can provide sufficient carbon and nitrogen source to further increase the performance as LIBs' anodes.

In this study, we report ZnO/ZnFe₂O₄/N-doped C micro-polyhedrons with hierarchical hollow structure (ZZFO-C) obtained through annealing of the bi-metallic ZIF-ZnFe (molar ratio of 3:1) MOF

precursor. The resulting material has high surface area and is constituted by the organized assembly of numerous subunit-nanoparticles with a size of around 20 nm. For comparison purposes, the porous micro-polyhedron ZnO/ZnFe₂O₄ (ZZFO) material is also synthesized by a different calcination method.

2. Experimental section

2.1. Chemicals

Zinc nitrate hexahydrate (Zn(NO₃)₂·6H₂O, 98%) was obtained from Alfa Aesar Chemical Co. Iron(II) sulfate heptahydrate (FeSO₄·7H₂O, 99%), 2-methylimidazole (99%) and polyvinylpyrrolidone (PVP, K-30, 99%) were purchased from Sigma-Aldrich Chemical Co. Methanol (dried, 0.003% H₂O) was obtained from SeccoSolvTM.

2.2. Synthesis of ZIF-ZnFe

In a typical synthesis of the ZIF-ZnFe precursor, 476 mg (1.6 mmol) of Zn(NO₃)₂·6H₂O and 111.2 mg (0.4 mmol) of FeSO₄·7H₂O were dissolved into 50 mL of methanol to form Solution-A. 2-methylimidazole (656.8 mg, 8 mmol) and PVP (600 mg) were added to 50 mL of methanol to prepare Solution-B. Then, using a constant pressure funnel, Solution-A was dropped into Solution-B while stirring. After complete mixing, the solution was aged at room temperature for 24 h. The formed yellow precipitate was separated by centrifugation, washed with methanol for five times, and dried in the oven at 60 °C overnight to obtain the precursor, ZIF-ZnFe, as a yellow powder.

2.3. Preparation of the ZZFO-C and ZZFO products

First, the ZIF-ZnFe powder was pre-heated to 400 °C for 2 h with a ramp of 2 °C min⁻¹ under nitrogen flow in a tube furnace to favour the carbon formation. After cooling, the material was annealed for 2 h (heating ramp 10 °C min⁻¹) in a muffle furnace (i.e., in air) either at 500 °C to get the hollow structured ZZFO-C, or 650 °C to obtain porous ZZFO instead.

2.4. Material characterization

The powder X-ray diffraction (XRD) pattern was recorded in a Bragg-Brentano geometry on a Bruker D8 Advance diffractometer (Cu-K α radiation, λ = 0.154 nm) over the 5–90° (2 θ) range. The morphology and structure of all samples was investigated via field-emission scanning electron microscopy (SEM, ZEISS 1550VP) and transmission electron microscopy (TEM, JEOL JEM-3000). The lattice fringes were determined via Cs-corrected high-resolution transmission electron microscopy operated at an acceleration voltage of 80 and 300 kV (FEI Titan 80–300 kV). X-ray photoelectron spectroscopy (XPS) measurements were conducted on a PHI 5800 MultiTechnique ESCA System with monochromatized Al-K α (1486.6 eV) radiation at a take-off angle of 45°, using pass energies at the analyzer of 29.35 eV or 93.9 eV for detail and survey scans, respectively. An electron flood gun was used to compensate sample charging during the measurement. For BE calibration, the main C1s peak was set to 284.8 eV. Peak fitting was done with the CasaXPS software using Shirley background subtraction and mixed Gaussian-Lorentzian peak shapes. Raman characterization was performed with a confocal InVia Raman micro spectrometer with a 633 nm laser (Renishaw; each spectrum was taken as the average of three, 10-s accumulations). Thermo-gravimetric analysis (TGA) was performed using a thermogravimetric analyzer (TA Instruments, Model Q5000) at a heating rate of 5 °C min⁻¹ under N₂ or air flow. N₂ absorption-desorption isotherms of samples were determined and analyzed by the Brunauer-Emmette-Teller (BET) method (Autosorb-iQ, Quantachrome). The metal content of the obtained samples was determined via inductively coupled plasma optical emission spectroscopy (ICP-OES). The

samples were dissolved into hot hydrochloric acid (HCl) and analyzed using the Spectro Arcos (Spectro Analytical Instruments) with axial plasma view. CHN elemental analysis was also conducted (Elementar vario MICRO cube).

2.5. Electrochemical characterization

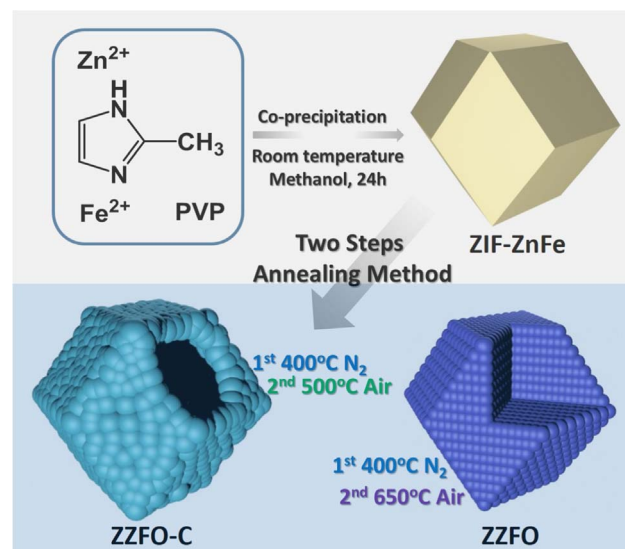
The working electrodes based on ZZFO-C and ZZFO consisted of 70 wt% active material, 25 wt% conductive carbon (Super C45, TIMCAL) and 5 wt% sodium carboxymethyl cellulose (CMC, Dow Wolff Cellulosics). To prepare the working electrodes, first the binder (CMC) was dissolved in deionized water to obtain a 5 wt% solution. A proper amount of such a solution was mixed with the conductive carbon in a mortar. Then, the active material was added to the mixture and further ground for 2 h in the same mortar. The resulting slurry was casted onto dendritic copper foil by the doctor blade technique, with a wet film thickness of 100 μm . The coated electrodes were dried at room temperature, punched to form disk electrodes (12 mm in diameter), which were further dried for 24 h at 120 $^{\circ}\text{C}$ under vacuum. The active material mass loading of the electrodes was between 1.0 and 1.2 mg cm^{-2} . These relatively low mass loadings were chosen because of the high theoretical capacity of the active materials. The electrochemical characterization was performed in three-electrode Swagelok-type cells with lithium metal (Rockwood Lithium, battery grade) for the reference and counter electrodes. The cells were assembled in an Ar-filled glove-box with O_2 and H_2O content below 0.5 ppm. A 1 M solution of LiPF_6 in ethylene carbonate (EC) - diethyl carbonate (DEC) (1:1 by volume, UBE) with 1% vinylene carbonate (VC) served as electrolyte. All the potential values in this manuscript refer to the Li/Li^+ quasi-reference couple. All tests were performed at 20 ± 2 $^{\circ}\text{C}$. Galvanostatic cycling and rate-capability performance tests were performed in the potential range from 0.01 to 3.0 V using a battery tester (Maccor 4300). Cyclic voltammetries were recorded within the same potential range using a programmable potentiostat (VMP3, Biologic Science Instruments).

2.6. In situ XRD analysis

In situ XRD analysis of ZZFO-C was performed via a self-designed, in-situ cell (two-electrode) [12,19]. The working electrode slurry, consisting of 65 wt% active material, 25 wt% super-C45, and 10 wt% CMC, was casted onto a beryllium (Be) disk (wet thickness of 250 μm). The working electrode was dried at 50 $^{\circ}\text{C}$ under vacuum overnight. Lithium foil served as the counter electrode, while two layers of glass fiber (GF/D, Whatman) soaked with around 300 μL of the electrolyte were used as separators. The assembled in-situ cell was left to rest (OCV) for 12 h before starting each experiment. Galvanostatic charge and discharge tests were performed using a potentiostat/galvanostat (SP-150, BioLogic) applying a current density of 40 mA g^{-1} with the 0.01–3.0 V voltage range. Meanwhile, XRD diffractograms were recorded in the 25–80 $^{\circ}$ (2 θ) range with a time per scan of 1883.6 s (about 30 min).

3. Results and discussion

ZZFO-C and ZZFO were synthesized by annealing bimetallic ZIF-ZnFe at different temperatures, as clearly displayed in Scheme 1. The ZIF-ZnFe precursor (with Zn/Fe molar ratio of 2.97 according to the ICP results reported in Table S1) was prepared via the simple stirring and aging of the methanol solution containing 2-methylimidazole and PVP with Zn^{2+} and Fe^{2+} ions. As shown by the SEM images in Fig. 1a and b, the obtained bimetallic ZIFs is constituted by uniform microcrystals of quasi polyhedral shape with an average size of about 500 nm. Fig. 1b reveals that the surface of the polyhedron is relatively smooth. However, compared with the previously reported ZIF-8 [27,28], additional nanoparticles (size of ~ 50 nm) and nanosheets appear to have grown on the surface of the sub-micrometric polyhedron, maybe due to Fe ion



Scheme 1. Schematic illustration of the ZZFO-C and ZZFO synthesis.

doping (according to preliminary data collected on a series of MOFs with varying Zn-Fe molar ratio, not reported here for sake of brevity). The elemental mapping image (see Fig. S1) of the ZIF-ZnFe supports the uniform dispersion of four elements (Zn, Fe, C and N). Interestingly, as shown in Fig. 1c, TEM clearly reveals the solid inner structure of ZIF-ZnFe without any obvious porosity. Detailed information about the crystal structure was obtained through powder-XRD (see Fig. 1d), which shows all of the characteristic reflections of ZIF-8 (JCPDS card no. 62-1030), without additional features deriving from impurities and, thus, confirming that the bimetallic ZIF-ZnFe possesses a phase-pure ZIF-8 structure.

In order to preserve the original structure of the precursor, a two steps annealing method was developed to form oxides of the transition metals. In the first step, the ZIF-ZnFe precursor was pre-heated via annealing at 400 $^{\circ}\text{C}$ in nitrogen. Then, the annealed precursor was calcined in air to obtain the final product [29–31]. In this way, the carbon formed in the pre-heating step acts as temporary buffer preventing the frameworks to collapse in the following calcination step [11,29–31]. The thermogravimetric analysis (TGA) data of the pre-heated precursor recorded under air flow is exhibited in Fig. S2. As noticeable, the weight increases in the temperature range comprised between 120 to 300 $^{\circ}\text{C}$, as result of the formation of the metal oxides. Afterwards, the preheated ZIF-ZnFe undergoes an obvious weight loss in the temperature range between 300 $^{\circ}\text{C}$ and 650 $^{\circ}\text{C}$ and a tiny plateau is also observed at about 480–500 $^{\circ}\text{C}$. The weight loss in this region can be attributed to the carbonization of the organic linkers and degradation of preheated ZIF-ZnFe [11,29–31]. The XRD patterns of the products obtained after annealing at different temperatures in air flow are shown in Fig. S3. ZnO is the first metal oxide formed (at 300 $^{\circ}\text{C}$). When increasing the temperature to 350 $^{\circ}\text{C}$, new reflections appear related to the formation of Fe_2O_3 . Above 400 $^{\circ}\text{C}$, the new phase ZnFe_2O_4 started to develop while, at 450 $^{\circ}\text{C}$ no presence of Fe_2O_3 is observed any more. These results confirm that ZnO and Fe_2O_3 convert into ZnFe_2O_4 at temperatures near 450 $^{\circ}\text{C}$, which is in agreement with the plateau observed at ca. 480–500 $^{\circ}\text{C}$ in the TGA (see Fig. S2) [5]. Based on these results, we selected 500 $^{\circ}\text{C}$ as the annealing temperature for the synthesis of $\text{ZnO/ZnFe}_2\text{O}_4$ composite materials (ZZFO-C).

The phase and structure of the ZZFO-C obtained after the two-step annealing was investigated by XRD. Fig. 2 displays the Rietveld refinement of the ZZFO-C powder pattern, indicating the material to be a mixture of spinel ZnFe_2O_4 ($Fd-3m\bar{S}$ space group with $a = 8.4302610(30)$ \AA) and hexagonal ZnO ($P6_3mc$ space group with $a = 3.2527005(12)$ \AA and $c = 5.2069964(19)$ \AA). The refinement has been

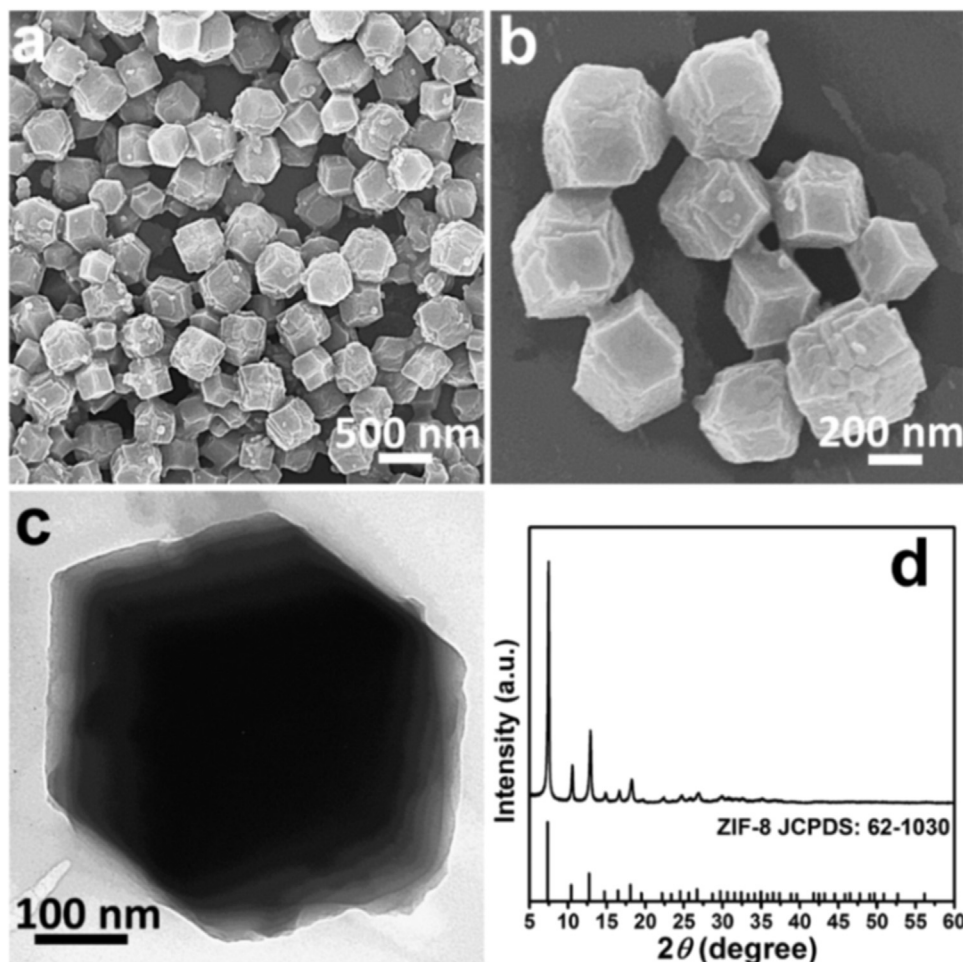


Fig. 1. Morphological and structural characterization of ZIF-ZnFe; a)–b) SEM images; c) HRTEM image; d) XRD pattern.

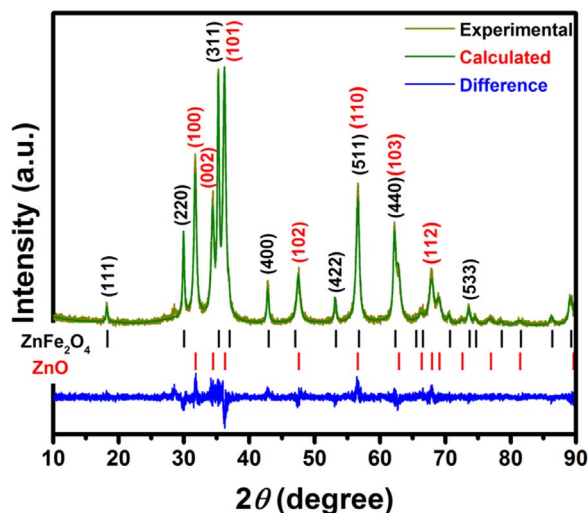


Fig. 2. The Rietveld refinement and powder X-ray diffraction patterns of the ZZFO-C composite materials.

performed with satisfactory agreement factors ($R_{wp} = 13.09\%$, $R_p = 9.87\%$, goodness of fit = 1.12) (ICSD $ZnFe_2O_4$: 28511, ZnO : 180050). No other reflections from impurities can be observed in XRD pattern. More detailed information about the chemical compositions and chemical state of ZZFO-C were gathered by X-ray photoelectron spectroscopy (XPS). The XP spectra in Fig. 3a reveal the presence of Zn, Fe, O, C, and N in ZZFO-C (the presence of sulfur is probably due to some residual SO_4^{2-}). The detail spectrum in the C 1s region (Fig. 3b) can be

fitted by three peaks at binding energies of 284.8, 286.4, and 288.7 eV, which are assigned to the carbon atoms of $C=C/C-C/C-H$, $C-O/C-N$, and $O-C=O$ functionalities, respectively [32,33]. Two peak components can be observed in the N 1s detail spectrum (Fig. 3c) at 398.7 and 400.3 eV, which represent pyridinic and pyrrolic nitrogen atoms in the nitrogen-doped ZZFO-C [33]. The spectrum in the O 1s region (in Fig. 3d) can be resolved into two components centered at 530.2 and 531.4 eV, which can be ascribed to the oxygen in metal oxides and to C-coordinated oxygen in the ZZFO-C composite [34]. Fig. 3e shows the Fe 2p spectrum. Here the two features at 711.1 and 724.3 eV are the Fe $2p_{3/2}$ and $2p_{1/2}$ peaks, with the shakeup satellites appearing at 717.4 and 730.6 eV, which indicates the presence of Fe(III) in $ZnFe_2O_4$ [5,8]. Finally, two features were detected in the Zn 2p spectrum (Fig. 3f) at 1021.4 and 1044.5 eV representing the Zn $2p_{3/2}$ and $2p_{1/2}$ peak components. While the peak position of the Zn 2p peaks is known to be not a direct indicator for the Zn oxidation state, the calculated Auger parameter (i.e., the sum of the Zn $2p_{3/2}$ peak binding energy and the kinetic energy of the Zn $L_{3M_{45}M_{45}}$ Auger peak, also detected in the XP spectra, but not shown for the sake of brevity) of 2010.5 eV points to an oxidation state of Zn(II) in ZZFO-C [5,8]. Based on the above XRD and XPS results, the ZIF-ZnFe was completely transformed upon annealing into the hybrid composite of ZnO and $ZnFe_2O_4$, but containing several oxygen functional groups and nitrogen-doped carbon species.

The morphology and structure of ZZFO-C were further investigated by field-emission scanning electron microscopy (FESEM) and transmission electron microscopy (TEM). Interestingly, the images in Fig. 4a and b show that ZZFO-C well retained the original micro-polyhedron shape of the ZIF-ZnFe precursor, although a slight decrease in particle size is observed (the average size is ~ 420 nm) associated to partial

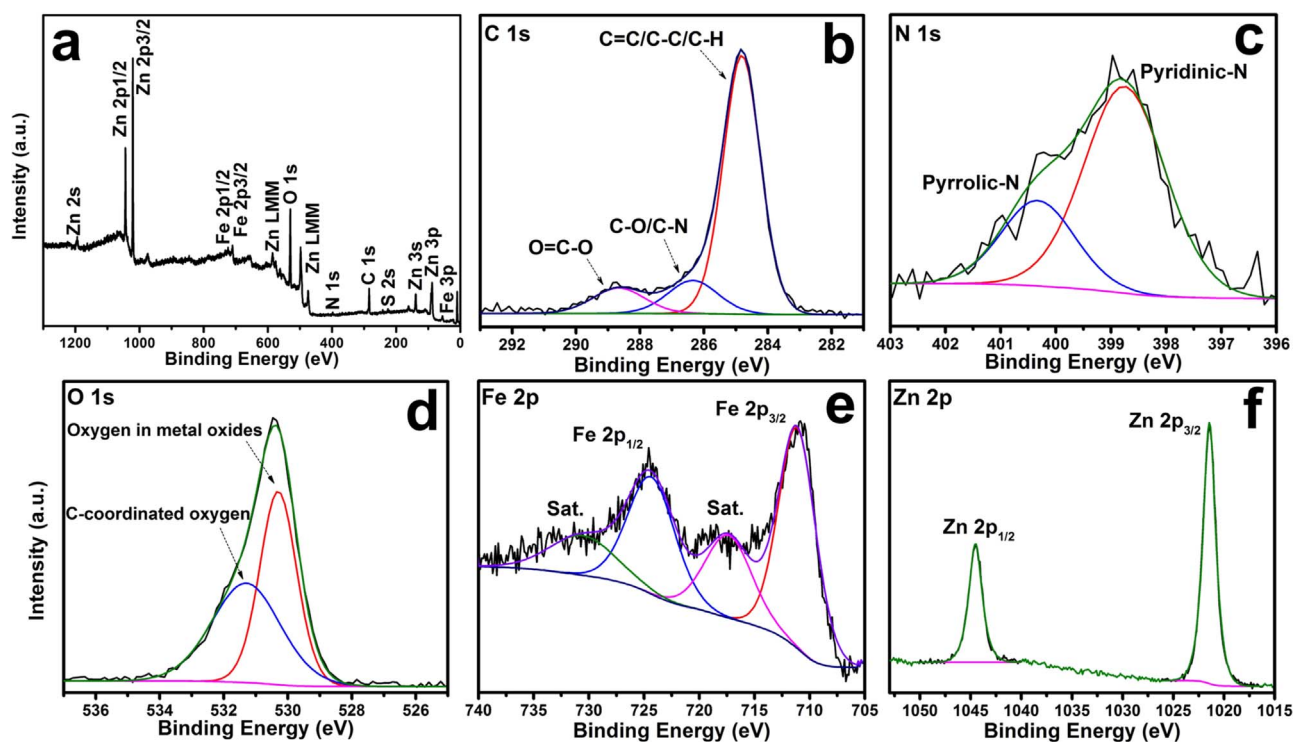


Fig. 3. XPS spectra and fitted data of the obtained ZZFO-C: a) survey spectrum, b) C 1s, c) N 1s, d) O 1s, e) Fe 2p, and d) Zn 2p spectra.

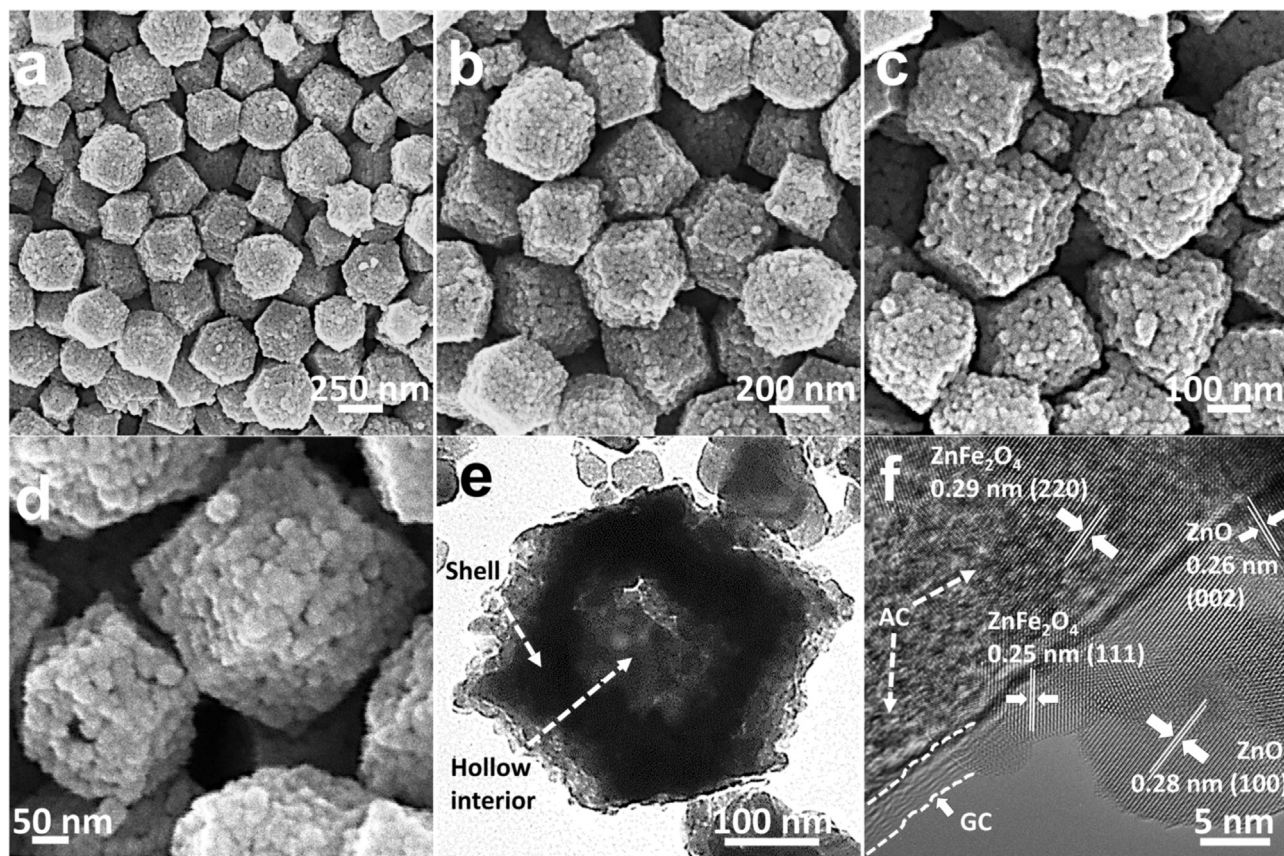


Fig. 4. Morphological and structural characterization of as-obtained ZZFO-C: a)–d) FESEM images with different magnifications; e)–f) HRTEM images. AC: amorphous carbon; GC: graphitized carbon.

decomposition and contraction of the framework during the heating process. Interestingly, the SEM images recorded at higher magnifications (Fig. 4c and d) reveal that the surface of ZZFO-C is relatively rougher than the parental compound, and composed of clustered metal oxides/carbon composite nanoparticles with a size of about 20 nm and numerous small holes. Furthermore, the TEM image (Fig. 4e) reveals an obvious contrast between the dark outer shell and the lighter large cavity in the ZZFO-C micro-polyhedron. The shell is clearly constituted by many nanoparticles in agreement with the SEM image in Fig. 4d. According to previous reports, the cause for the formation of a hollow structure is the non-equilibrium annealing treatment leading to a great temperature gradient along the radial direction. This results in the initial formation of metal oxides particles on the surface. Then the inner ZIF-ZnFe is gradually decomposed to form gaseous products (e.g., CO_2 , H_2O and NO_2) that escape leading to the formation of a porous shell and a hollow structure [13,24,35–37]. The high-resolution TEM images of ZZFO-C clearly evidence the lattice fringes and carbon layer. The d -spacings of 0.29 and 0.25 nm are assigned to the (220) and (111) crystalline planes of cubic spinel ZnFe_2O_4 , while values of 0.28 and 0.26 nm belong to the (100) and (002) lattice planes of hexagonal ZnO. The carbon layer is obviously constituted by two parts, an amorphous carbon layer (AC) and some more graphitized carbon (GC) at the edge [8,12,13,38]. The ZnO/ ZnFe_2O_4 nanoparticles and the carbon layers obviously overlap with each other, indicating the coexistence of an extensive carbon matrix on the metal oxides in ZZFO-C. The energy dispersive spectrometer (EDS) mapping images of ZZFO-C (see Fig. S4) further confirm the coexistence of five elements, the EDS images show the homogeneous distribution of C, N, O, Zn, and Fe within ZZFO-C. Thus, based on the above results, the obtained ZZFO-C is confirmed to be a ZnO/ ZnFe_2O_4 /N-doped C composite material with a unique hierarchical hollow structure.

When the 2nd annealing step temperature is increased to 650 °C, the obtained product is still composed of ZnO and ZnFe_2O_4 (according to the Rietveld refinement of powder XRD pattern in Fig. S5). However, less or no carbon is left (based on TGA of ZZFO, see Fig. S8), therefore this sample is denoted as ZZFO. Compared to ZZFO-C, the SEM and TEM images of ZZFO display distinct variations in morphology and structure. As shown in Fig. 5a–c, ZZFO still maintains the original micro-polyhedron shape of the precursor, with a rough surface and a particle diameter of about 350 nm. Interestingly though, the inner cavities observed in ZZFO-C are not present in ZZFO. Furthermore, the porous structure of ZZFO seems to be constituted by smaller nanoparticles (\leq about 10 nm) and numerous holes (see TEM image in Fig. 5d). We propose that the decomposition of the carbon matrix leads to the further breaking of the framework followed by contraction of the whole structure, which leads to decreased size of the micro-polyhedron and nano-subunits, as well as the disappearance of the inner cavity [13]. Certainly, the complete understanding of morphological and structural changes occurring upon annealing at increasing temperatures needs to be further investigated. Nevertheless, it is clear that the annealing temperature plays a crucial role for tuning the structure and morphology of these materials. When annealing at even higher temperatures (i.e., 800 °C), for example, the initial micro-polyhedron shape of the parent ZIF-ZnFe particles is fully lost (see SEM images in Fig. S6), and the resulting product is a mixture of particles with irregular shape and size [13].

The Raman spectrum (see Fig. S7) of ZZFO-C shows two bands at 1344 and 1578 cm^{-1} , ascribed to the D and G bands of the carbon matrix [12,39]. On the contrary, the same bands are not observed for ZZFO, indicating the substantial absence of carbon in the sample annealed at higher temperature. Next, the TGA (see Fig. S8) further proves the presence of ca. 15 wt% carbon and nitrogen in ZZFO-C, while the TGA curves of ZZFO does not show any obvious weight loss from 40 to 800 °C under air flow. In Table S1 the elemental content (determined by ICP-OES and CHN analysis) of the precursor, ZZFO-C, and ZZFO is summarized. The specific surface area (SSA) of the ZIF-ZnFe precursor,

ZZFO-C and ZZFO was estimated using the Brunauer-Emmette-Teller (BET) theory (see isotherms in Fig. S9a). The ZIF-ZnFe precursor shows the largest surface area of 980.7 $\text{m}^2 \text{g}^{-1}$, which is substantially decreased upon conversion into metal oxides. ZZFO-C and ZZFO possess, in fact, surface areas of 84.3 and 31.2 $\text{m}^2 \text{g}^{-1}$, respectively. The smallest value of ZZFO is attributed to the lack of inner cavities, as well as the absence of carbon. The pore size distribution calculated through the Barrett-Joyner-Halenda (BJH) method (see Fig. S9b) reveals the mesoporous character of the obtained ZZFO-C and ZZFO, with average pore sizes around 13 and 39 nm, respectively. These pores may derive from the escape of gases during the decomposition of the organic ligand in the annealing process. Such mesoporous features can assist the transport of Li^+ and, most important, buffer the volume variation during repeated insertion/deinsertion.

In Fig. 6, the cyclic voltammeteries (CV) of a ZZFO-C-based electrode were recorded over a potential range from 0.01 to 3.0 V. During the initial cathodic sweep, the very first small peak A (1.43 V) could be assigned to the intercalation of Li^+ into ZnFe_2O_4 . Then, three obvious peaks can be observed at around 0.84 (B), 0.74 (C), and 0.44 V (D), which can be ascribed to the decomposition of ZnO and ZnFe_2O_4 to form Zn^0 , Fe^0 , and Li_2O . Meanwhile, peak C can be also attributed to the formation of the solid electrolyte interphase (SEI) [19]. Below 0.3 V, Peak E is generally assigned to the alloying reaction of Zn^0 and Li^0 , charge accumulation and Li ion insertion into the carbon. In the following anodic scan, three broad peaks (F, G, and H) can be observed, indicating the stepwise de-alloying reaction of Li-Zn alloys, and the re-oxidation of Zn and Fe, respectively [12,19,40]. Upon subsequently cycling, the cathodic sweeps show only three features around 1.0, 0.44 and < 0.3 V. The anodic scan does not show substantially change instead. This behavior confirms the remarkable reversibility of the ZZFO-C composite [19].

In order to further unveil the electrochemical reaction mechanism, in situ XRD measurements were performed during the first galvanostatic charge/discharge cycle (at 40 mA g^{-1}) [12,19,41]. The collected XRD patterns and the respective voltage profile are shown in Fig. 7. Based on the features of the potential profile (Fig. 7a and b) and CV wave (Fig. 6), an eight-section reaction mechanism may be postulated for the ZZFO-C anode. Fig. 7c presents an overview of the XRD patterns evolution (130 scans) resulting from the structural and phase changes. Accordingly, these are grouped into eight sections emphasized by the red scans in Fig. 7c. In region A, the voltage profile rapidly declined from the OCV to around 1.3 V, then decrease slowly down to 1.0 V. Although the (440) reflection of ZnFe_2O_4 slightly shifts to lower 2θ values, the XRD patterns in region A (scan 1–4) do not change substantially (Fig. 7d). As previously mentioned along with the CV discussion, Li^+ mainly intercalates into ZnFe_2O_4 in this voltage region [12]. In region B (from 1.0 to 0.84 V), the diffraction patterns (scan 4–11) evidence a rapid intensity decrease for the ZnFe_2O_4 reflection, until completely vanishing between scans 9 and 10. A slight intensity decrease is simultaneously observed for the ZnO reflections, meanwhile a new series of XRD peaks (at 36.5°, 42.5° and 61.6°) evolve gradually. These results suggest that, in region B, ZnFe_2O_4 completely converts into the oxygen-poor ZnFe_2O_w and amorphous Li_2O , also originating from the partial conversion (reduction) of ZnO [12,19]. In region C (from 0.84 to 0.7 V), the voltage profile exhibits a distinct plateau which corresponds to the reduction peak at around 0.74 V in the CV curve (signed C in Fig. 6). The XRD patterns (scans 11–28) reveals the reflections of oxygen-poor phase (ZnFe_2O_w) to continuously decrease until vanishing at scan 28. A gradual decrease in intensity of ZnO's reflections is also observed in this region, however coupled with the rise of a new broad reflection in the region comprised between 40° and 45°. As shown in our previous in situ XRD studies of ZnFe_2O_4 and ZnO anode by Bresser et al. and Mueller et al., respectively, in this potential window (0.84–0.7 V), the complete conversion of ZnFe_2O_4 into Zn^0 , Fe^0 and amorphous Li_2O can be expected. Meanwhile, the partial reduction of ZnO into Zn^0 and Li_2O also occurs, as suggested by the growing broad

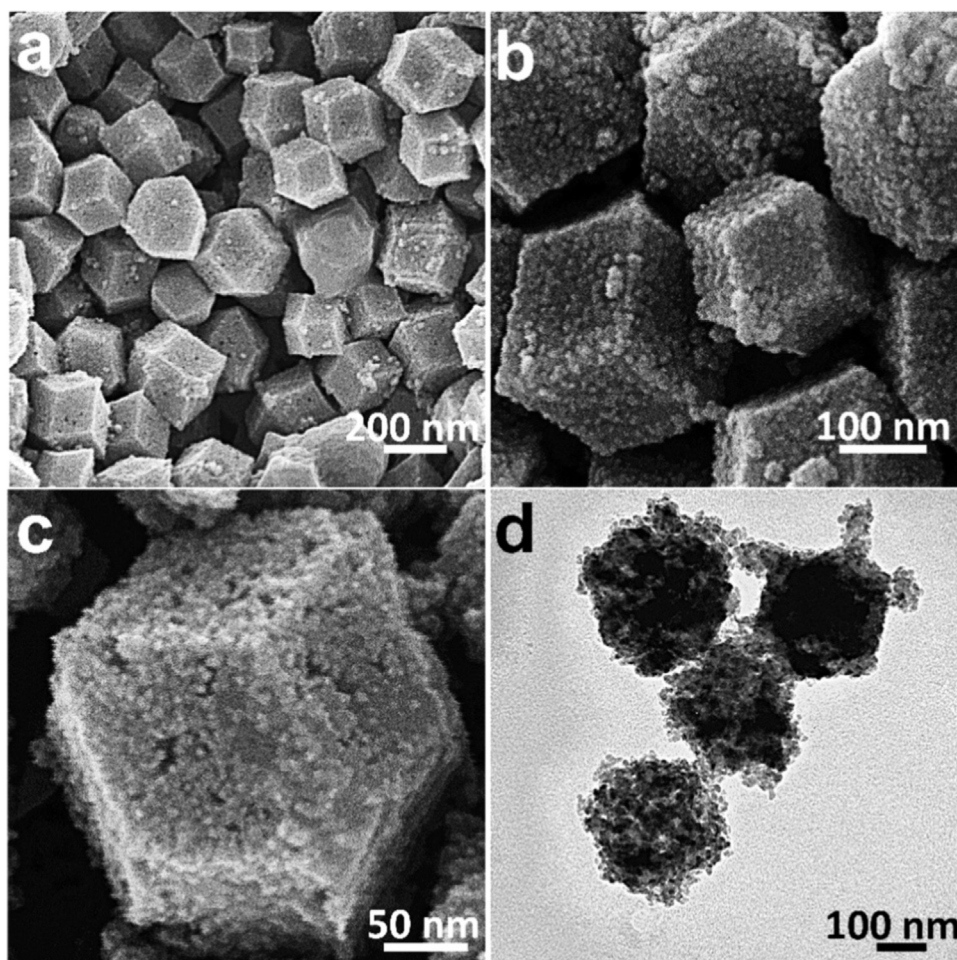


Fig. 5. Morphological and structural characterization of ZZFO; a)–c) FESEM images with different magnifications; d) HRTEM image.

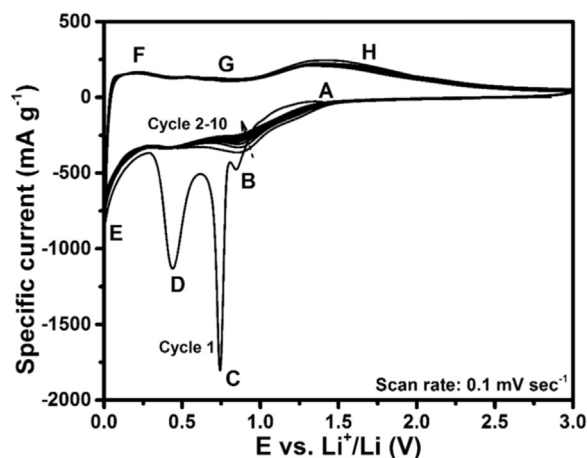


Fig. 6. Cyclic voltammetry of ZZFO-C electrode during the initial ten cycles. Scan rate 0.1 mV s^{-1} .

reflection presumably due to the formation of metallic Zn (at $\approx 43^\circ$) [12,19]. Upon further discharge (region D, from 0.7 to 0.4 V), a long plateau (corresponding to the peak occurring at 0.44 V in the CV) is observed. The XRD patterns recorded in region D (scan 28–53) reveal the continuous growth of the broad reflection in the region between 40.0° to 45.0° . Meanwhile, two new reflections appear at around 41.3° , and 42.8° corresponding to the LiZn_4 (scan 50–53) [19,42,43], while the ZnO-related features rapidly decrease until fully vanishing at scans 50–53. The XRD results for region D indicate the simultaneous occurrence of two reactions: (i) the complete decomposition of ZnO to form

Zn^0 and Li_2O and (ii) the alloying reaction of Zn with Li^+ to form LiZn_4 [19,43,44]. From 0.4 to 0.01 V, region E (scan 53–81), the voltage profile exhibits a less steep voltage slope corresponding to the last cathodic peak (signed E) observed in the CV at about 0.01 V. According to our previous work, in this potential region, Li^+ ions gradually combine with Zn to form the LiZn -alloy [12,19]. Here, the peak intensity of LiZn_4 (at around 42.8°) continuously decrease upon lithiation, whereas a new reflection at about 41.4° gradually evolves and shifts to lower 2θ values. When the anode is fully discharged to 0.01 V (scan 81), this new feature moves to 41° , which suggests the formation of the LiZn phase (JCPDS card no. 03-065-3016) [19]. As previously reported in literature, the alloying reaction between Li and Zn undergoes successive multi-step phase transformation such as: $\text{Zn} \rightarrow \text{LiZn}_4 \rightarrow \text{Li}_2\text{Zn}_5 \rightarrow \text{LiZn}_2 \rightarrow \text{Li}_2\text{Zn}_3 \rightarrow \text{LiZn}$ [42,43].

Upon delithiation, i.e., in region F (from 0.01 to 0.75 V), the alloy-related reflections decrease and shift to larger 2θ values, meanwhile the features of LiZn_4 reappear at the original position (see scan 92–93). Compared with region E, the obtained XRD patterns in region F reveal the reverse behavior, indicating the multistep de-alloying reaction: $\text{LiZn} \rightarrow \text{Li}_2\text{Zn}_3 \rightarrow \text{LiZn}_2 \rightarrow \text{Li}_2\text{Zn}_5 \rightarrow \text{LiZn}_4$ [42,43]. When the electrode is further delithiated to 1.2 V (region G, scan 93–103), the reflections of Zn^0 can be observed again. However LiZn_4 seems not to be entirely transformed into Zn^0 . Upon full delithiation up to 3.0 V (i.e., region H scan 103–130), a new broad reflection gradually evolves in the region comprised between 31° and 38° , coupled with an even broader feature evolving between 55° and 60° . The XRD patterns also reveal that no LiZn_4 is present in the electrode at complete recharge. Based on our previous works [12,19], these two new broad reflections can be likely attributed to the re-oxidation process of metallic Zn^0 and Fe^0 to form

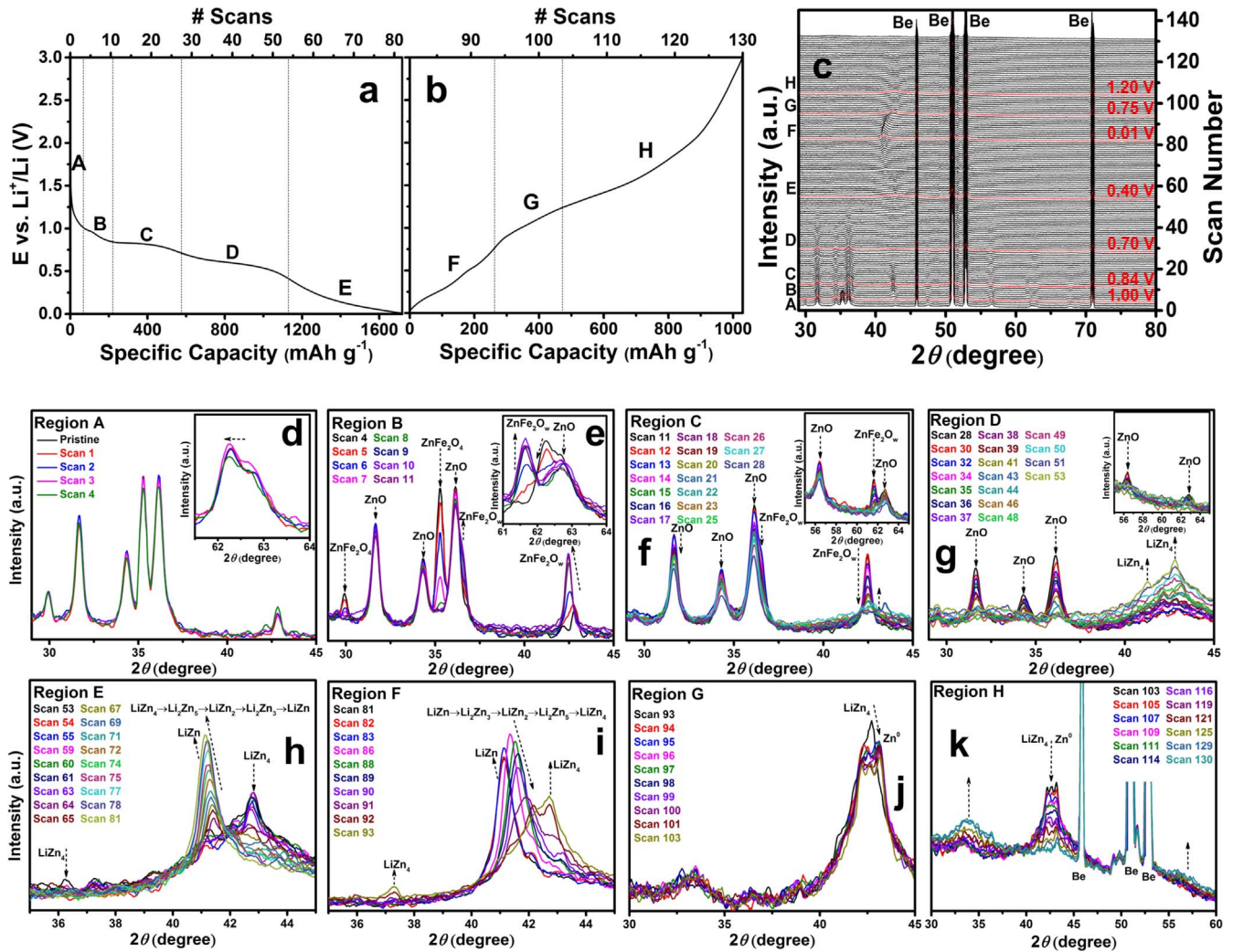


Fig. 7. In situ XRD measurements of ZZFO-C: a)–b) potential profile of the initial (de-)lithiation of ZZFO-C, c) in situ XRD patterns upon discharge/charge (scans 1–130), d)–k) details on the evolution of the XRD patterns.

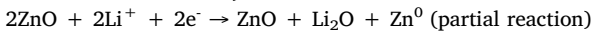
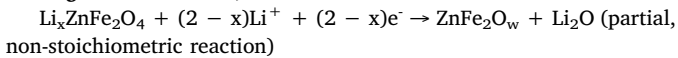
metal oxides, such as ZnO and Fe₂O₃ and, possibly, also to a mixture of ZnO, Fe₂O₃ and Zn_yFe_{2+y}O₄ ($y \leq 1$). Unfortunately, the substantial crystallinity decrease after the initial cycle, associated with the dramatic structural reorganization of the material, hinders an accurate characterization of the de-lithiated phase.

According to the above-discussed results, we can summarize the reaction mechanism for ZZFO-C anode during 1st discharge/charge process, not considering the Li⁺ insertion into carbon, as it follows:

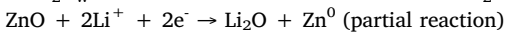
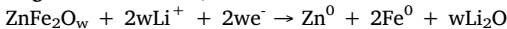
Region A (OCV–1.0 V, intercalation)



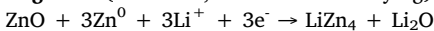
Region B (1.0–0.8 V, conversion)



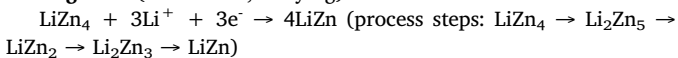
Region C (0.8–0.7 V, conversion)



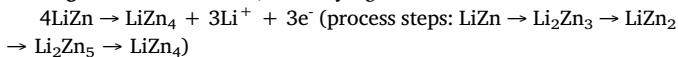
Region D (0.7–0.4 V, conversion & alloying)



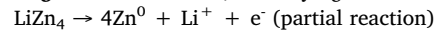
Region E (0.4–0.01 V, alloying)



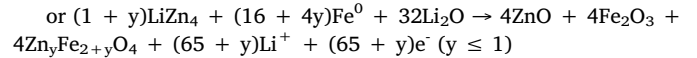
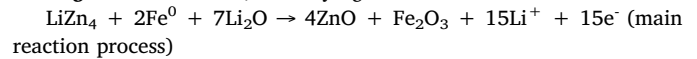
Region F (0.01–0.75 V, de-alloying)



Region G (0.75–1.2 V, de-alloying)



Region H (1.2–3.0 V, de-alloying & conversion)



With its unique hollow hierarchical structure, ZnO/ZnFe₂O₄/N-doped C (ZZFO-C) is expected to show high specific capacity and outstanding rate capability. These were indeed verified by galvanostatic cycling experiments. Fig. 8 shows the cycling performance of ZZFO-C and ZZFO at constant current density of 200 mA g⁻¹ in the potential range from 0.01 to 3.0 V. As displayed in Fig. 8a, the specific capacity delivered during the initial lithiation are 1751 mA h g⁻¹ and 1801 mA h g⁻¹ for ZZFO-C and ZZFO, respectively, resulting on a coulombic efficiency of 67.4% and 60.8%, respectively (see Fig. 8b). The initial capacity loss can be mostly ascribed to the partial irreversibility of the conversion reactions (see above) and the formation of the solid-electrolyte interphase (SEI) layer on the surface of the active particles [6,44]. Interestingly, despite having a larger BET area (see Fig. S9), the ZZFO-C electrode presents higher coulombic efficiency than ZZFO. This suggests that the main contribution to the irreversible capacity in the initial cycle does not arise from SEI formation, but rather from irreversibility of the conversion reaction. The presence of N-doped carbon matrix probably enhances this reversibility in the ZZFO-C

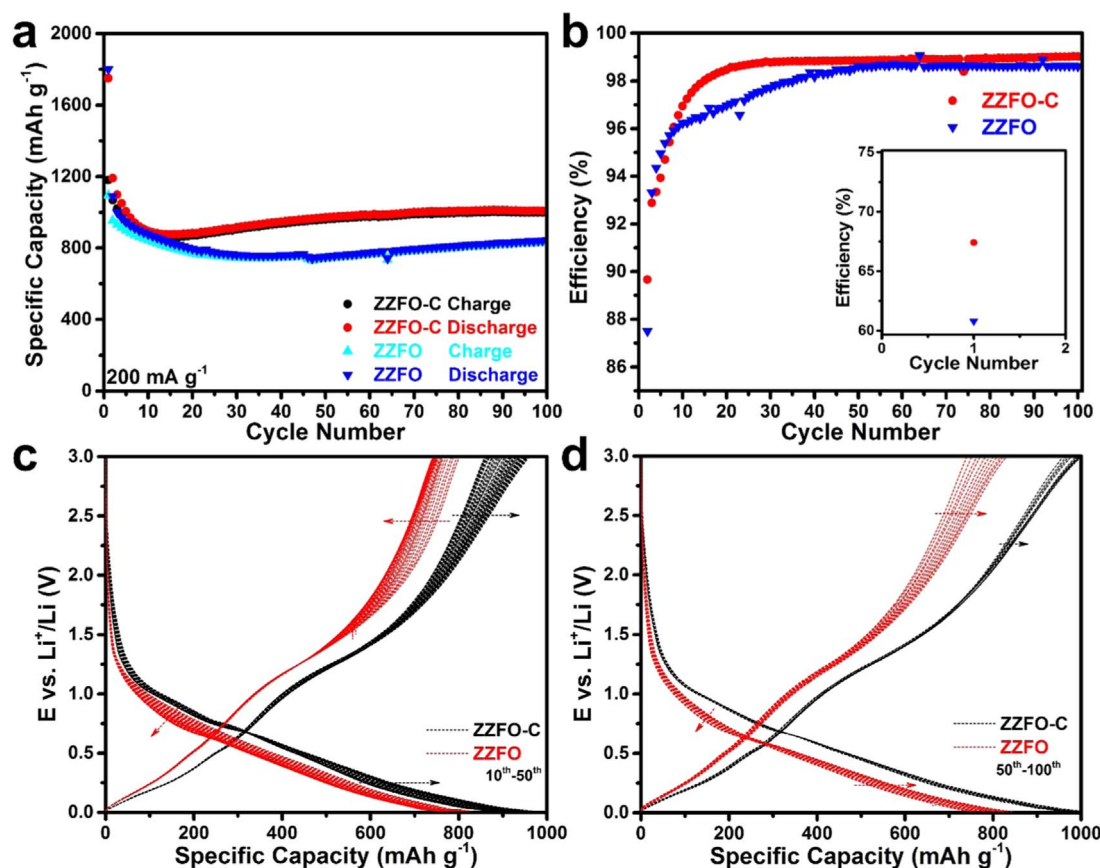


Fig. 8. Long term galvanostatic cycling of ZZFO-C and ZZFO electrodes. (Dis-)charge capacity (a) and coulombic efficiency (b) vs. cycle number at a current density of 200 mA g⁻¹. The corresponding voltage profiles of ZZFO-C and ZZFO for selected cycles (c: 10th–50th, d: 50th, 60th, 70th, 80th, 90th, 100th).

electrode. The generally poor first cycle efficiency, in line with other reports on MOF-derived metal oxides, evidences that this aspect needs further optimization [5,6,8,13]. Nevertheless, ZZFO-C shows a relatively large 1st cycle reversible capacity of 1180 mA h g⁻¹, which is substantially higher than that of ZZFO (1095 mA h g⁻¹). This could be attributed to the enhanced electronic conductivity provided by the nitrogen-doped carbon matrix and to the better electrolyte accessibility of ZZFO-C (void polyhedrons) [5,13,41,45]. Both ZZFO and ZZFO-C show a certain capacity fading in the first cycles due to the instable SEI layer and lithiation-induced mechanical degradation [13,46]. Nonetheless, from the 15th cycle, the specific capacity of ZZFO-C gradually increased to finally stabilize around 1000 mA h g⁻¹ at the 100th cycle. After 100 cycles, ZZFO-C still delivered stable capacity with ~ 1000 mA h g⁻¹ until the 130th cycle (see Fig. S11). Such a capacity increase upon cycling of metal oxide anodes has been ascribed to the reversible formation of a polymeric gel-like SEI layer on the active particles' surface [12,13,46]. The coulombic efficiency also increases to 98% at the 15th cycle and, finally, to 99% at the 50th cycle (see Fig. 8b). On the other hand, ZZFO always showed a lower coulombic efficiency of 98.3%, suggesting for the improved stability of the SEI grown on ZZFO-C [13,46]. Comparing the ex-situ TEM images of ZZFO-C and ZZFO (in Fig. S10) after the 70th galvanostatic cycle (at 200 mA g⁻¹) clearly evidences the reason for such an improved performance. In fact, ZZFO-C still shows the presence of the shell, the hollow features and the original shape, although the inner void space is reduced upon repeated lithiation. This is not the case of ZZFO, for which no obvious porous structure was detected after repeated lithiation cycles. Moreover, as shown in Fig. S12a, the long-cycling (dis-)charge stability under a high current density of 2000 mA g⁻¹ was evaluated too. Despite the initial capacity fading already observed at low current, the reversible capacity of the ZZFO-C anode appears relatively stable after the initial 30 cycles,

with more than 700 mA h g⁻¹ delivered at the 200th cycle. Contrarily, the ZZFO anode can only provide 412 mA h g⁻¹. Most importantly, after 200 cycles at 2000 mA g⁻¹, ZZFO-C displays the MOF-derived micro-polyhedrons quite well retaining their original shape, while in ZZFO they appear partially broken (see ex situ SEM images in Fig. S12b and c).

This difference is also observed in the potential profiles of selected cycles of ZZFO-C and ZZFO (Fig. 8c and d). The gradually increasing polarization of the ZZFO electrode (indicated by the red short dash arrow on the discharge curves in Fig. 8c) is the reason for the observed capacity degradation. Although it stabilizes and decreases in later cycles (Fig. 8d), the polarization of the ZZFO electrode is always higher than that of the ZZFO-C one. This arises from the better electrolyte accessibility granted by the preserved hollow structure of ZZFO-C and the wettability of the N-doped carbonaceous percolating network [1,12,19,40,41,45]. More importantly, in the charge profiles (in Fig. 8c and d), ZZFO-C shows larger capacity arising from the alloying mechanism (below 1.2 V) and improved reversibility of the Li₂O formation (above 1.5 V).

Fig. 9a and b displays the rate capability of ZZFO-C and ZZFO tested by increasing the current density from 50 to 2000 mA g⁻¹ every 10 cycles (excluded the activation cycles 1st–3rd at 20 mA g⁻¹). ZZFO-C showed an excellent rate capability with the average specific capacities being 1075, 1052, 1024, 928, 842, and 787 mA h g⁻¹ at current density of 50, 100, 200, 500, 1000, and 1500 mA g⁻¹, respectively. Even at 2000 mA g⁻¹, the electrode delivered a very high specific capacity (750 mA h g⁻¹). Remarkably, ZZFO-C could afterwards recover its initial performance with 1190 mA h g⁻¹ at 100 mA g⁻¹ in the 75th cycle. As previously observed, the specific capacity then continuously increased upon cycling to reach 1328 mA h g⁻¹ at the 90th cycle. ZZFO showed substantially inferior performance, with 840, 775, 644, 523,

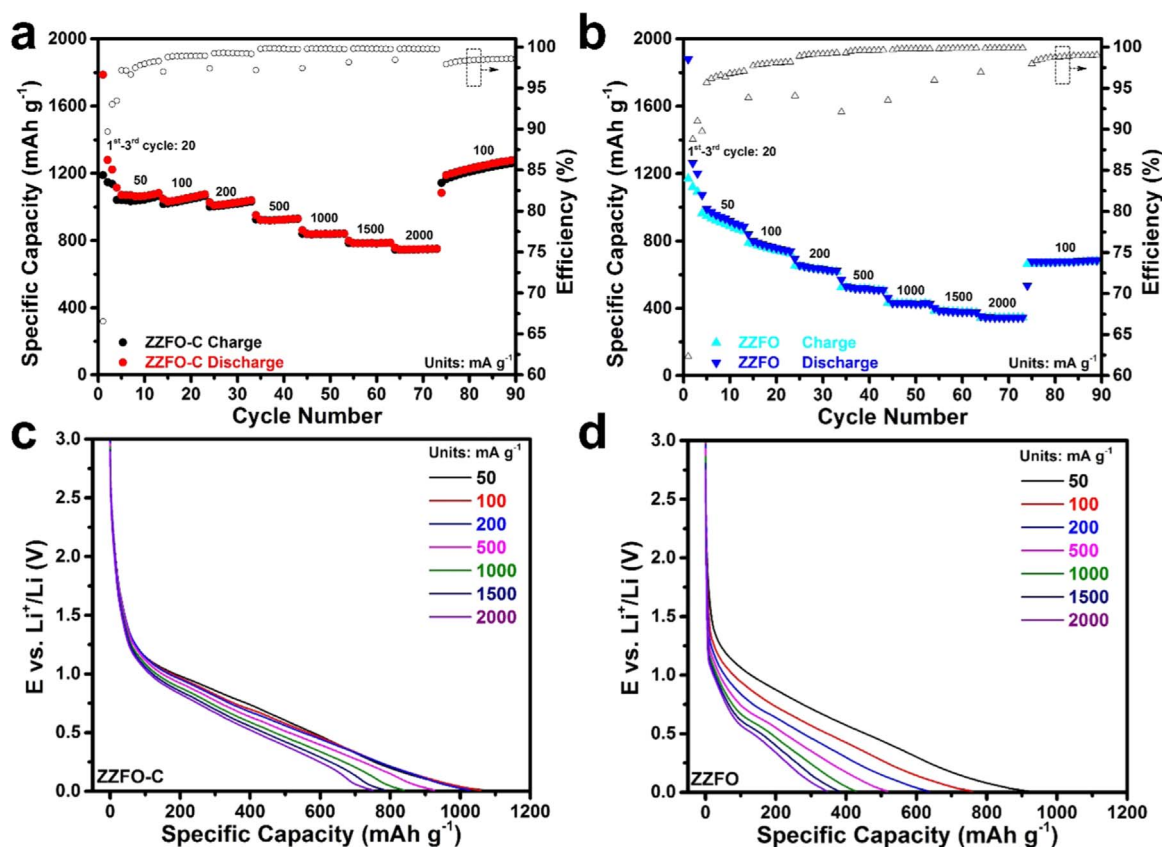


Fig. 9. Rate capability of the ZZFO-C (a) and ZZFO (b) anodes at different specific currents from 20 to 2000 mA g⁻¹. The corresponding discharge voltage profiles of ZZFO-C (c) and ZZFO (d) for selected cycles (10th, 20th, 30th, 40th, 50th, 60th, 70th).

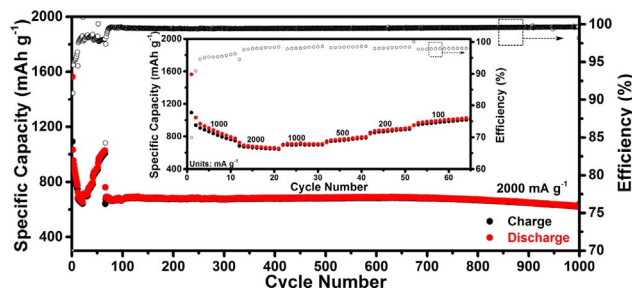


Fig. 10. Rate capability test for ZZFO-C-based anodes at various current rates (1st–65th cycles) and long cycling galvanostatic measurement for ZZFO-C anodes (66th–1000th cycles).

433, 384 and 347 mA h g⁻¹ delivered at 50, 100, 200, 500, 1000, 1500, and 2000 mA g⁻¹, respectively. After the rate was decreased to 100 mA g⁻¹, ZZFO also recovered the discharge capacity of 679 mA h g⁻¹ (at 75th cycle), but without any increase upon cycling. Additionally, ZZFO showed higher initial voltage drops at higher rates with respect to ZZFO-C (compare panel c and d in Fig. 9), indicating that the N-doped carbon matrix improves the high rate performance, and increases significantly the cycling stability as well as the capacity retention after the elevated C rate test.

The long-term high rate performance of ZZFO-C electrode was further investigated at the highest current density of (2000 mA g⁻¹; see Fig. 10). Interestingly, ZZFO-C still exhibits a very promising long-term performance, as evidenced by the stable capacity (about 680 mA h g⁻¹) delivered at 2000 mA g⁻¹ for more than 700 cycles (see Fig. 10). After 1000 cycles the electrode retained 92.5% of the capacity detected at the 66th cycle (670.49 mA h g⁻¹).

4. Conclusion

In summary, we have successfully developed the hierarchical hollow structure including transition metal oxide ZnO/ZnFe₂O₄/N-doped C (ZZFO-C micro-polyhedrons) via a self-sacrificial template method involving the calcination of a bi-metallic MOFs (ZIF-ZnFe) precursor. Carbon-free porous ZnO/ZnFe₂O₄ micro-polyhedrons (ZZFO) have also been obtained changing annealing condition. Excitingly, ZZFO-C-based electrode shows an improved electrochemical performance compared to ZZFO, thanks to the unique hollow structure and improved conductivity as well as stability arising from the N-doped carbon matrix. ZZFO-C exhibited a large reversible capacity of 1000 mA h g⁻¹ after 100 cycles at specific current of 200 mA g⁻¹ and outstanding rate capability. Even after undergoing high-rate testing (2.0 A g⁻¹), ZZFO-C still showed excellent reversibility delivering a stable capacity of 620 mA h g⁻¹ after 1000 cycles.

Acknowledgements

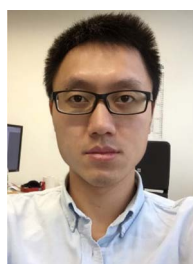
The authors thank Dr. Dominic Bresser for the valuable discussions. Y.M., Y.J.M., and H.Z. gratefully acknowledge financial support from the Chinese Scholarship Council (CSC). Financial support from the Helmholtz Association is also acknowledged. Furthermore, the authors would like to thank Yuanchun Ji for TEM testing.

Appendix A. Supplementary material

Supplementary data associated with this article can be found in the online version at <http://dx.doi.org/10.1016/j.nanoen.2017.11.030>.

References

- [1] D. Bresser, S. Passerini, B. Scrosati, Leveraging valuable synergies by combining alloying and conversion for lithium-ion anodes, *Energy Environ. Sci.* 9 (2016) 3348–3367.
- [2] C. Yuan, H.B. Wu, Y. Xie, X.W. Lou, Mixed transition-metal oxides: design, synthesis, and energy-related applications, *Angew. Chem. Int. Ed.* 53 (2014) 1488–1504.
- [3] B. Scrosati, J. Garche, Lithium batteries: status, prospects and future, *J. Power Sources* 195 (2010) 2419–2430.
- [4] J.-M. Tarascon, M. Armand, Issues and challenges facing rechargeable lithium batteries, *Nature* 414 (2001) 359–367.
- [5] L. Hou, L. Lian, L. Zhang, G. Pang, C. Yuan, X. Zhang, Self-sacrifice template fabrication of hierarchical mesoporous bi-component-active ZnO/ZnFe₂O₄ sub-microcubes as superior anode towards high-performance lithium-ion battery, *Adv. Funct. Mater.* 25 (2015) 238–246.
- [6] S.J. Yang, S. Nam, T. Kim, J.H. Im, H. Jung, J.H. Kang, S. Wi, B. Park, C.R. Park, Preparation and exceptional lithium anodic performance of porous carbon-coated ZnO quantum dots derived from a metal–organic framework, *J. Am. Chem. Soc.* 135 (2013) 7394–7397.
- [7] X. Gu, L. Chen, Z. Ju, H. Xu, J. Yang, Y. Qian, Controlled growth of porous α -Fe₂O₃ branches on β -MnO₂ nanorods for excellent performance in lithium-ion batteries, *Adv. Funct. Mater.* 23 (2013) 4049–4056.
- [8] F. Zou, X. Hu, Z. Li, L. Qie, C. Hu, R. Zeng, Y. Jiang, Y. Huang, MOF-derived porous ZnO/ZnFe₂O₄/C octahedra with hollow interiors for high-rate lithium-ion batteries, *Adv. Mater.* 26 (2014) 6622–6628.
- [9] J. Li, J. Wang, D. Wexler, D. Shi, J. Liang, H. Liu, S. Xiong, Y. Qian, Simple synthesis of yolk-shelled ZnCo₂O₄ microspheres towards enhancing the electrochemical performance of lithium-ion batteries in conjunction with a sodium carboxymethyl cellulose binder, *J. Mater. Chem. A* 1 (2013) 15292–15299.
- [10] G. Zhang, L. Yu, H.B. Wu, H.E. Hoster, X.W. Lou, Formation of ZnMn₂O₄ ball-in-ball hollow microspheres as a high-performance anode for lithium-ion batteries, *Adv. Mater.* 24 (2012) 4609–4613.
- [11] X. Xu, R. Cao, S. Jeong, J. Cho, Spindle-like mesoporous α -Fe₂O₃ anode material prepared from MOF template for high-rate lithium batteries, *Nano Lett.* 12 (2012) 4988–4991.
- [12] D. Bresser, E. Paillard, R. Kloepsch, S. Krueger, M. Fiedler, R. Schmitz, D. Baither, M. Winter, S. Passerini, Carbon coated ZnFe₂O₄ nanoparticles for advanced lithium-ion anodes, *Adv. Energy Mater.* 3 (2013) 513–523.
- [13] F. Zheng, M. He, Y. Yang, Q. Chen, Nano electrochemical reactors of Fe₂O₃ nanoparticles embedded in shells of nitrogen-doped hollow carbon spheres as high-performance anodes for lithium-ion batteries, *Nanoscale* 7 (2015) 3410–3417.
- [14] Z. Wu, W. Ren, L. Xu, F. Li, H. Cheng, Doped graphene sheets as anode materials with super high rate and large capacity for lithium ion batteries, *ACS Nano* 5 (2011) 5463–5471.
- [15] X. Ge, Z. Li, C. Wang, L. Yin, Metal–organic frameworks derived porous core/shell structured ZnO/ZnCo₂O₄/C hybrids as anodes for high-performance lithium ion battery, *ACS Appl. Mater. Interfaces* 7 (2015) 26633–26642.
- [16] M. Li, Y.X. Yin, C. Li, F. Zhang, L.J. Wan, S. Xu, D.G. Evans, Well-dispersed bi-component-active CoO/CoFe₂O₄ nanocomposites with tunable performances as anode materials for lithium-ion batteries, *Chem. Commun.* 48 (2012) 410–412.
- [17] G. Li, W. Li, K. Xu, R. Zou, Z. Chen, J. Hu, Sponge-like NiCo₂O₄/MnO₂ ultrathin nanoflakes for supercapacitor with high-rate performance and ultra-long cycle life, *J. Mater. Chem. A* 2 (2014) 7738–7741.
- [18] A.K. Rai, J. Gim, T.V. Thi, D. Ahn, S.J. Cho, J. Kim, High rate capability and long cycle stability of Co₃O₄/CoFe₂O₄ nanocomposite as an anode material for high-performance secondary lithium ion batteries, *J. Phys. Chem. C* 118 (2014) 11234–11243.
- [19] F. Mueller, D. Geiger, U. Kaiser, S. Passerini, D. Bresser, Elucidating the impact of cobalt doping on the lithium storage mechanism in conversion/alloying-type zinc oxide anodes, *ChemElectroChem* 3 (2016) 1311–1319.
- [20] H. Furukawa, K.E. Cordova, M. O’Keeffe, O.M. Yaghi, The chemistry and applications of metal-organic frameworks, *Science* 341 (2013) 1230444.
- [21] O.M. Yaghi, H. Li, Hydrothermal synthesis of a metal-organic framework containing large rectangular channels, *J. Am. Chem. Soc.* 117 (1995) 10401–10402.
- [22] W. Xia, A. Mahmood, R. Zou, Q. Xu, Metal-organic frameworks and their derived nanostructures for electrochemical energy storage and conversion, *Energy Environ. Sci.* 8 (2015) 1837–1866.
- [23] Y. Ma, H. Ma, Z. Yang, J. Ma, Y. Su, W. Li, Z. Lei, Methyl cinnamate-derived fluorescent rigid organogels based on cooperative π – π stacking and C=O \cdots π interactions instead of H-bonding and alkyl chains, *Langmuir* 31 (2015) 4916–4923.
- [24] L. Zhang, H.B. Wu, S. Madhavi, H.H. Hng, X.W. Lou, Formation of Fe₂O₃ microboxes with hierarchical shell structures from metal–organic frameworks and their lithium storage properties, *J. Am. Chem. Soc.* 134 (2012) 17388–17391.
- [25] G. Huang, L. Zhang, F. Zhang, L. Wang, Metal-organic framework derived Fe₂O₃@NiCo₂O₄ porous nanocages as anode materials for Li-ion batteries, *Nanoscale* 6 (2014) 5509–5515.
- [26] Z. Li, B. Li, L. Yin, Y. Qi, Prussian blue-supported annealing chemical reaction route synthesized double-shelled Fe₂O₃/Co₃O₄ hollow microcubes as anode materials for lithium-ion battery, *ACS Appl. Mater. Interfaces* 6 (2014) 8098–8107.
- [27] J. Tang, R.R. Salunkhe, J. Liu, N.L. Torad, M. Imura, S. Furukawa, Y. Yamauchi, Thermal conversion of core–shell metal–organic frameworks: a new method for selectively functionalized nanoporous hybrid carbon, *J. Am. Chem. Soc.* 137 (2015) 1572–1580.
- [28] N.L. Torad, M. Hu, Y. Kamachi, K. Takai, M. Imura, M. Naito, Y. Yamauchi, Facile synthesis of nanoporous carbons with controlled particle sizes by direct carbonization of monodispersed ZIF-8 crystals, *Chem. Commun.* 49 (2013) 2521–2523.
- [29] R. Wu, X. Qian, K. Zhou, J. Wei, J. Lou, P.M. Ajayan, Porous spinel Zn_xCo_{3–x}O₄ hollow polyhedra templated for high-rate lithium-ion batteries, *ACS Nano* 8 (2014) 6297–6303.
- [30] R.R. Salunkhe, J. Tang, Y. Kamachi, T. Nakato, J.H. Kim, Y. Yamauchi, Asymmetric supercapacitors using 3D nanoporous carbon and cobalt oxide electrodes synthesized from a single metal-organic framework, *ACS Nano* 9 (2015) 6288–6296.
- [31] X. Cao, B. Zheng, X. Rui, W. Shi, Q. Yan, H. Zhang, Metal oxide-coated three-dimensional graphene prepared by the use of metal-organic frameworks as precursors, *Angew. Chem.* 126 (2014) 1428–1433.
- [32] X. Dou, I. Hasa, M. Hekmatfar, T. Diemant, R.J. Behm, D. Buchholz, S. Passerini, Pectin, hemicellulose, or lignin? Impact of the biowaste source on the performance of hard carbons for sodium ion batteries, *ChemSusChem* 10 (2017) 2668–2676.
- [33] A.L.M. Reddy, A. Srivastava, S.R. Gowda, H. Gullapalli, M. Dubey, P.M. Ajayan, Synthesis of nitrogen-doped graphene films for lithium battery application, *ACS Nano* 4 (2010) 6337–6342.
- [34] S. Lu, H. Wang, J. Zhou, X. Wu, W. Qin, Atomic layer deposition of ZnO on carbon black as nanostructured anode materials for high-performance lithium-ion batteries, *Nanoscale* 9 (2017) 1184–1192.
- [35] J. Zhong, C. Cao, Y. Liu, Y. Li, W.S. Khan, Hollow core-shell g-Fe₂O₃ microspheres with excellent lithium-storage and gas-sensing properties, *Chem. Commun.* 46 (2010) 3869–3871.
- [36] L. Zhou, H. Xu, H. Zhang, J. Yang, S.B. Hartono, K. Qian, J. Zou, C. Yu, Cheap and scalable synthesis of α -Fe₂O₃ multi-shelled hollow spheres as high-performance anode materials for lithium ion batteries, *Chem. Commun.* 49 (2013) 8695–8697.
- [37] H.B. Lin, H.B. Rong, W.Z. Huang, Y.H. Liao, L.D. Xing, M.Q. Xu, X.P. Li, W.S. Li, Triple-shelled Mn₂O₃ hollow nanocubes: force induced synthesis and excellent performance as the anode in lithium-ion batteries, *J. Mater. Chem. A* 2 (2014) 14189–14194.
- [38] J. Cai, C. Wu, Y. Zhu, P.K. Shen, K. Zhang, Hierarchical porous acetylene black/ZnFe₂O₄/carbon hybrid materials with high capacity and robust cycling performance for Li-ion batteries, *Electrochim. Acta* 187 (2016) 584–592.
- [39] S. Sanchez-Valdes, A.G. Zapata-Dominguez, J.G. Martinez-Colunga, J. Mendez-Nonell, L.F. Ramos de Valle, A.B. Espinoza-Martinez, A. Morales-Cepeda, T. Lozano-Ramirez, P.G. Lafleur, E. Ramirez-Vargas, Influence of functionalized polypropylene on polypropylene/graphene oxide nanocomposite properties, *Polym. Compos.* (2016), <http://dx.doi.org/10.1002/pc.24077>.
- [40] F. Mueller, D. Bresser, E. Paillard, M. Winter, S. Passerini, Influence of the carbonaceous conductive network on the electrochemical performance of ZnFe₂O₄ nanoparticles, *J. Power Sources* 236 (2013) 87–94.
- [41] D. Bresser, F. Mueller, M. Fiedler, S. Krueger, R. Kloepsch, D. Baither, M. Winter, E. Paillard, S. Passerini, Transition-metal-doped zinc oxide nanoparticles as a new lithium ion anode material, *Chem. Mater.* 25 (2013) 4977–4985.
- [42] Y. Hwa, J.H. Sung, B. Wang, C. Park, H. Sohn, Nanostructured Zn-based composite anodes for rechargeable Li-ion batteries, *J. Mater. Chem.* 22 (2012) 12767–12773.
- [43] M. Park, G. Sung, N. Sung, J. Kim, C. Park, Partially reversible Li₂O formation in ZnO: a critical finding supporting realization of highly reversible metal oxide electrodes, *J. Power Sources* 328 (2016) 607–614.
- [44] L. Qie, W. Chen, Z.H. Wang, Q.G. Shao, X. Li, L.X. Yuan, X.L. Hu, W.X. Zhang, Y.H. Huang, Nitrogen-doped porous carbon nanofiber webs as anodes for lithium ion batteries with a super high capacity and rate capability, *Adv. Mater.* 24 (2012) 2047–2050.
- [45] D. Bresser, E. Paillard, P. Niehoff, S. Krueger, F. Mueller, M. Winter, S. Passerini, Challenges of “Going Nano”: enhanced electrochemical performance of cobalt oxide nanoparticles by carbothermal reduction and in situ carbon coating, *ChemPhysChem* 15 (2014) 2177–2185.
- [46] H. Sun, G. Xin, T. Hu, M. Yu, D. Shao, X. Sun, J. Lian, High-rate lithiation-induced reactivation of mesoporous hollow spheres for long-lived lithium-ion batteries, *Nat. Commun.* 5 (2014) 4526.



Yuan Ma is a Ph.D. candidate in Physical Chemistry at Helmholtz Institute Ulm (HIU), Karlsruhe Institute of Technology (KIT) in Germany under the supervision of Prof. Stefano Passerini and Dr. Alberto Varzi. He received his B.Sc. in Chemistry (2012) and M.Sc. degrees in Macromolecular Chemistry and Physics (2015) from Northwest Normal University (NWNNU), China. Currently, his research interests focus on the synthesis and characterization of transition metal oxide/sulfide-carbon composite electrode materials for lithium and sodium ion batteries.



Yanjiao Ma is currently pursuing her Ph.D. under the supervision of Professor Stefano Passerini and Dr. Dominic Bresser at Helmholtz Institute Ulm (HIU); affiliated with the Karlsruhe Institute of Technology, KIT) in Germany, where she is studying nanostructured active materials for lithium-based batteries. Prior to this, she received her M.S. from Northwest Normal University (NWNNU) under the supervision of Professor Rongfang Wang in China, investigating nanomaterials and their application as electrocatalysts. She is co-author of 17 scientific papers (h-index of 10), 6 Chinese licensed patents.



Thomas Diemant is a postdoctoral research fellow at the Institute of Surface Chemistry and Catalysis at Ulm University. He received his Ph.D. degree from Ulm University in 2008. His research interests include studies on the structural, electronic and chemical properties of bimetallic model catalyst surfaces under ultra-high vacuum (UHV) conditions and the characterization of heterogeneous catalysts, nano-materials and electrochemical energy conversion and storage materials by X-ray photoelectron spectroscopy (XPS).



Dorin Geiger is a senior scientist in the Materials Science Electron Microscopy Facility at Ulm University, Germany. He studied Physics and received his Ph.D. degree in 2001 from the Eberhard Karls University of Tübingen, Germany, in the field of High Resolution Transmission Electron Microscopy and Electron Holography on high-Tc superconductive materials. He worked till 2011 at the Triebenberg Laboratory for Electron Microscopy and Electron Holography of the Technical University Dresden with the focus on High Resolution Cs-Corrected Electron Holography.



R. Jürgen Behm is Professor of Physical Chemistry at Ulm University in Ulm/Germany. After receiving his Ph.D. in chemistry 1980 from the Ludwig-Maximilians-University in Munich he was awarded a post-doctoral fellowship at the IBM Research Laboratory in San José/USA. In 1987 he became Professor at the Ludwig-Maximilians-University in Munich, in 1992 he was appointed as full professor of Physical Chemistry at Ulm University. He is a fellow of the International Society of Electrochemistry (ISE). His research interests focus on the microscopic, molecular-scale understanding of catalytic/electrocatalytic processes at the solid-gas and solid-liquid interface, with emphasis on energy related processes.



Ute Kaiser studied physics and crystallography at the Humboldt University Berlin and received from there her Diploma degree in 1976 and her doctoral degree in 1993; her habilitation in experimental physics she received from Jena University in 2002. From 1976 to 1991 she was scientific co-worker at the Academy of Science in Jena and from 1991–2004 scientific assistant at the Jena University. Since 2004 she is a full professor at Ulm University and head of the Central Facility of Materials Science Electron Microscopy. She is working on development and application of advanced electron microscopy techniques to understand the material's physical properties from the atomic scale.



Alberto Varzi studied Chemistry of Materials at University of Bologna (Italy) and graduated in 2008. He continued his education in Germany and received a Ph.D. in 2013 from the Ulm University and ZSW. After a postdoctoral period at WWU Münster/MEET, he is now a senior scientist at the Helmholtz-Institute Ulm for Electrochemical Energy Storage of the Karlsruhe Institute for Technology. Currently his research interests are focused on materials for Lithium-ion, Lithium-Sulfur batteries and Supercapacitors.



Huang Zhang received his BS degree in 2010 in Polymer Materials from Jiangnan University and MS degree in 2013 in Materials Science from East China University of Science and Technology, China. Then, he had one-year research experience as predoctoral fellow in University of Leuven, Belgium. Currently, he is pursuing his Ph.D. in Physical Chemistry at Helmholtz Institute Ulm, Karlsruhe Institute of Technology in Germany under the supervision of Prof. Stefano Passerini. His research interests focus on the development of new materials for electrochemical energy storage.



Stefano Passerini is Professor at the Karlsruhe Institute of Technology. His research activities are focused on electrochemical energy storage with special focus on improving the sustainability of high-energy batteries. Co-author of more than 400 papers (Scopus H-Index: 65), a few book chapters and several international patents, he has been awarded the 2012 Research Award of the Electrochemical Society Battery Division.



Guk-Tae Kim received his Ph.D. degree in the Department of Ceramic Engineering at the Gyeongsang National University in 2004, and is, now working at the Helmholtz Institute Ulm (HIU) of the Karlsruhe Institute of Technology (KIT) in Germany. His main research activities are focused on the processing of electrode formulations in aqueous media as well as investigation of suitable binder systems, PEO-based solid polymer electrolyte and high-energy cathode materials for rechargeable lithium-ion batteries.